THE JOURNAL OF PHYSICAL CHEMISTRY C

Article

pubs.acs.org/JPCC

Vibrational Properties of Metal Phosphorus Trichalcogenides from First-Principles Calculations

Arsalan Hashemi,*[,†] Hannu-Pekka Komsa,*[,†] Martti Puska,[†] and Arkady V. Krasheninnikov[†,‡]

[†]Department of Applied Physics, Aalto University, P.O. Box 11100, 00076 Aalto, Finland

[‡]Helmholtz-Zentrum Dresden-Rossendorf, Institute of Ion Beam Physics and Materials Research, 01328 Dresden, Germany

ABSTRACT: Two-dimensional (2D) sheets of transition metal phosphorus trichalcogenides (TMPTs) offer unique magnetic and optical properties that can complement those found in other 2D materials. Insights into the structure and properties of these materials can be obtained by a juxtaposition of the experimental and calculated Raman spectra, but there is very little theoretical knowledge of the vibrational properties of TMPTs. Using first-principles calculations, we study mechanical and vibrational properties of a large set of monolayer TMPTs. From the phonon dispersion curves, we assess the dynamical stabilities and general trends on the atomic character of the vibrational modes. We determine Raman active modes from group theory, calculate Raman intensities, and analyze them with the help of the corresponding atomic displacements. We evaluate how the mode frequencies shift in response to a biaxial strain. We also determine elastic properties, which show that these systems are softer than many other layered materials. In addition to shedding light on the general features of vibrational properties of these materials, our results should also prove useful for interpreting experimental Raman spectra.

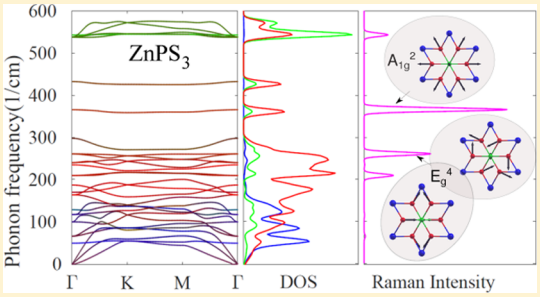

1. INTRODUCTION

In a quest to expanding the atlas of attainable physical properties of two-dimensional (2D) materials, the research community has started to revisit "old" van der Waals (vdW) layered structures, from which "new" 2D systems can be exfoliated. In this context, the family of transition metal phosphorus trichalcogenides (TMPTs) with a structural formula of MPX_3, where M = V, Mn, Fe, Co, Ni, Cd, Mg, Zn; X = S or Se, has recently started to attract interest, since the bulk TMPTs possess band gaps in a range of 1.3−3.5 eV, wider than those in transition metal dichalcogenides (TMDs), where the gaps do not exceed 2 eV. Besides, TMPTs exhibit magnetic ordering and can be exfoliated into single sheets.[1−6] Contrary to many metal chalcogenides, the constituent chemical elements are largely earth abundant and nontoxic. Moreover, as in the case of many layered materials, electronic and optical properties are sensitive to the number of layers, which opens additional degrees of freedom for engineering the electronic properties of these materials. For example, the observed band gap of bulk $NiPS_3$ is equal to 1.6 eV, while the exfoliation into the bilayer results in an indirect-to-direct band gap transition[7] with a value of the gap being 2.6 eV.

The atomic structure of TMPTs is similar to that of TMDs in the octahedral phase (T-phase) for the position of the metal and chalcogen atoms.[8,9] A difference is that one-third of the metal atoms is replaced by P_2 dimers oriented normal to the layer, as shown in Figure 1. Each $[P_2X_6]^{-4}$ unit occupies the center of the six closest divalent metal ions M^{+2} forming a hexagonal lattice. In addition to their role in defining the electronic structure, some of the metal elements in this family of compounds are magnetic (Fe, Ni, Mn, and Co). As the metal atoms form a hexagonal lattice, each with three neighbors, these structures can exhibit stable magnetic phases. Experimentally Néel and zigzag antiferromagnetic phases have been observed with strong intraplanar and weak interplanar coupling. In fact, these materials were investigated in the past as an attractive platform to study 2D magnetism.[10,11] The combination of a large band gap and magnetism are expected to find applications in optoelectronics, magneto-optics, and magnetic storage,[12−14] in addition to the applications often envisioned for layered materials, e.g., in electrochemistry.[15]

Although magnetic and electronic properties of the TMPT materials have been extensively studied, the vibrational properties of monolayer MPX_3 have been scarcely investigated up to now. At the same time, the transition into magnetic state as a function of temperature can be observed in Raman spectra.[16] In addition, Raman spectra can be used to assess, e.g., mechanical strain, doping, the number of layers, or concentration of defects in 2D materials.[17−21] Thus, the precise microscopic knowledge of the vibrational properties is important for analyzing the Raman spectra and the phonon properties affecting thermal transport.

To fill the gaps in the existing knowledge, in this work we perform first-principles calculations for the phonon spectra and Raman intensities of $MgPS_3$, $MgPSe_3$, $MnPS_3$, $MnPSe_3$, $FePS_3$, $FePSe_3$, $NiPS_3$, $NiPSe_3$, $ZnPS_3$, $ZnPSe_3$, $CdPS_3$, and $CdPSe_3$

Received: September 28, 2017
Revised: November 13, 2017
Published: November 13, 2017

DOI: 10.1021/acs.jpcc.7b09634
J. Phys. Chem. C 2017, 121, 27207−27217

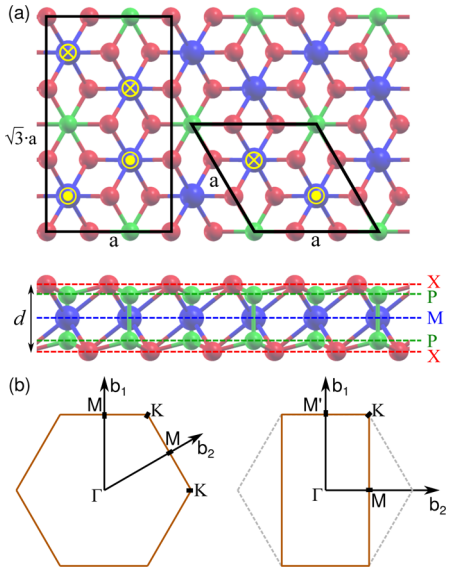

Figure 1. (a) Schematic representation of the atomic stucture of the MPX_3 monolayer, the top and side views. Blue, green, and red balls correspond to metal (M), phosphorus (P), and chalcogen (X) atoms, respectively. The rectangular unit cell and the hexagonal primitive cell are shown in the top view panel by black lines. The yellow markers ⊗ and ⊙ show the direction of magnetic moments, illustrating the zigzag AFM order in the rectangular unit cell and the Néel AFM order in the primitive cell. The thickness of the sheet is quantified using the parameter *d*, which is equal to the distance between chalcogen atoms in a single layer. Note that it is different from the unit cell length *c* in the bulk materials. (b) Sketch of the Brillouin zones for the hexagonal and rectangular unit cells, as well as the labeling adopted for the high-symmetry k-points used in the phonon dispersions plots.

compounds. To analyze the vibrational modes, we examine the ionic displacements and the contributions from different elements. We further calculate Raman intensities and frequency shifts upon application of biaxial strain. We also assess the mechanical properties of these systems by evaluating elastic constants. With the data obtained for a large set of TMPTs, we can extract the trends common for the whole family of these materials and compare our results to other 2D systems.

2. COMPUTATIONAL DETAILS

Density functional theory (DFT) calculations were performed in the framework of the projector augmented wave method using VASP[25] code. The plane wave basis set with a kinetic energy cutoff of 500 eV was used for all materials. Very tight convergence criteria are required in the calculation of phonon dispersion curves. To this end, the total energies in both geometry relaxation and in phonon calculations were converged within 10^{-7} eV and the forces to within 0.1 meV/Å.

The different materials considered in this work have different magnetic orders, which can require the use of unit cells of different sizes. Specifically, Mg, Cd, and Zn compounds are nonmagnetic (NM) due to the filling of the d shell of metal atoms. For the magnetic structures, the experimental results reveal the existence of two different models of magnetic moments ordering.[6,10,26] $MnPX_3$ shows a Néel antiferromagnetic (AFM) phase. Fe and Ni materials display zigzag AFM below the Néel temperatures. The determination of magnetic models is simplified by the fact that the magnetic moments originate almost entirely from the d electrons of the metals in the honeycomb lattice. Both the NM and the Néel AFM phases can be described using the hexagonal primitive cell containing 10 atoms. In the case of zigzag AFM phase, a larger tetragonal unit cell with 20 atoms needs to be adopted. These are both displayed in Figure 1. The 6 × 6 × 1 k-mesh was found to be sufficient for the Mg, Mn, Zn, and Cd compounds. $FePX_3$ and $NiPX_3$ require a larger 16 × 9 × 1 k-mesh.

For describing the exchange and correlation effects, we have chosen to adopt the functional proposed by Perdew, Burke, and Ernzerhof (PBE).[27] Calculated lattice parameters and layer thicknesses are compared with the experimental ones in Table 1.

Table 1. Calculated Monolayer and Experimental Bulk Lattice Constants *a*, Layer Thicknesses *d*, and Band Gaps E_g and Ground-State Magnetic Orders[a]

	a (Å)		*d* (Å)		E_g (eV)		magnetic GS
	PBE	expt.	PBE	expt.	PBE	expt.	PBE
$MgPS_3$	6.10	6.09	3.28	3.26	2.84(D)		NM
$MgPSe_3$	6.45	6.40	3.47	3.43	2.03(D)		NM
$MnPS_3$	6.05	6.08	3.23	3.21	1.33(I)	3.0	Néel AFM
$MnPSe_3$	6.39	6.38	3.34	3.28	0.99(I)	2.5	Néel AFM
$FePS_3$	5.86	5.95	3.12	3.19	0.12(I)	1.5	zigzag AFM
$FePSe_3$	6.22	6.27	3.29	3.17	0.11(I)	1.3	zigzag AFM
$NiPS_3$	5.82	5.81	3.03	3.21	0.70(I)	1.6	zigzag AFM
$NiPSe_3$	6.17	6.14	3.13	3.30	0.47(I)		zigzag AFM
$ZnPS_3$	6.01	5.97	3.23	3.20	2.14(I)	3.4	NM
$ZnPSe_3$	6.36	6.29	3.39	3.28	1.32(I)		NM
$CdPS_3$	6.30	6.21	3.41	3.38	1.93(I)	3.5	NM
$CdPSe_3$	6.62	6.51	3.58	3.25	1.29(I)		NM

[a]D/I after band gap value denotes direct/indirect gap. The experimental data is taken from refs 6, 11, and 22−24.

The experimental values correspond to the bulk systems. Table 1 also shows the calculated magnetic ground states, which were determined by comparing the total energies for four common magnetic moment orderings[28] and moreover found to agree with the experimental bulk magnetic orderings for all materials. The PBE results are in overall good agreement with the previous theoretical data[4,28] and the experimental values, although there appears to be an overestimation of the lattice constant in the case of $CdPX_3$ and an underestimation in the case for $FePX_3$, as well as underestimation of the layer thickness of $NiPX_3$. In addition, the lowest energy configuration of the $FePX_3$ compounds was accompanied by a strong structural distortion. The two Fe−Fe bond lengths along the zigzag chain became very different, 2.78 and 3.74 Å, for $FePS_3$ and 3.31 and 3.82 Å for $FePSe_3$, while they should be equal according to the experimentally determined crystal structures.[11,16] The problem may be related to the poor description of strong correlation effects among d-orbital electrons in some metals. This could be remedied, e.g., by the +*U* correction, but for the sake of consistency and also uncertainties in the choice of *U*, we generally refrain from adding +*U* corrections, and the results reported for $FePX_3$ correspond to the (metastable) symmetric structure. This yields Fe−Fe bond lengths of 3.32 and 3.52 Å for $FePS_3$ and $FePSe_3$, respectively. A comparison of the vibrational properties between the symmetric and distorted structures is given in the Appendix and discussed in more detail later on. The available experimental data on the band gaps of monolayer

DOI: 10.1021/acs.jpcc.7b09634
J. Phys. Chem. C 2017, 121, 27207−27217

Table 2. Character Tables of Irreducible Representations and Symmetry Operation Classes for D_{3d} and C_{2h} Point Symmetry Groups[31]

D_{3d}	E	$2C_3$	$3C_2$	i	$2S_6$	$3\sigma_h$	linear, rotations	quadratic
A_{1g}	1	1	1	1	1	1		$x^2 + y^2, z^2$
A_{2g}	1	1	−1	1	1	−1	R_z	
E_g	2	−1	0	2	−1	0	(R_x, R_y)	$(x^2 - y^2, xy)$ (xz, yz)
A_{1u}	1	1	1	−1	−1	−1		
A_{2u}	1	1	−1	−1	−1	1	z	
E_u	2	−1	0	−2	1	0	(x, y)	
C_{2h}	E	C_2		i	σ_h		linear, rotations	quadratic
A_g	1	1		1	1		R_z	x^2, y^2, z^2, xy
B_g	1	−1		1	−1		R_x, R_y	xy, yz
A_u	1	1		−1	−1		z	
B_u	1	−1		−1	1		x, y	

TMPTs are very limited. Comparison to bulk band gaps is shown in Table 1 and shows that the calculated values are consistently 1−1.5 eV lower. Quantitative comparison to calculations is hindered by the different number of layers as well as underestimation of band gaps calculated by PBE functional. Nevertheless, we can conclude that all these materials should be semiconductors.

The polarizability tensors for Raman calculations and the elastic constants were determined with the same parameters as above within the framework of the density functional perturbation theory (DFPT).[29] The lattice vibrations and dynamical stabilities were assessed using the PHONOPY code[30] within the supercell approach. Here, we used the finite displacement method instead of DFPT since, according to our calculations, it yields a better description of the flexural mode near the Γ-point. We used 6 × 6 × 1 supercells for the systems with the hexagonal primitive cells and 4 × 4 × 1 supercells for the tetragonal unit cell systems. In both cases, the Brillouin zone was sampled using the sole Γ-point.

3. RESULTS

3.1. Phonon Dispersions. The point symmetry group for dynamic configurations of nonmagnetic and Néel antiferromagnetic phases is D_{3d} (i.e., when M = Mg, Mn, Zn, or Cd). The character table, Table 2, for the triangular unit cell at the Γ-point predicts 30 vibrational modes corresponding to irreducible representations as $3A_{1g} + 2A_{2g} + 5E_g + A_{1u} + 4A_{2u} + 5E_u$. Five E_g and three A_{1g} modes are Raman-active, four E_u and three A_{2u} are IR-active, one A_{2u} and one E_u are acoustic, and A_{2g} and A_{1u} modes are optically inactive.

To analyze the vibrational properties of different modes, we start by showing phonon dispersion relations along the high-symmetry directions in the Brillouin zone and the phonon density of states (DOS) in Figure 2 and 3. The contributions from each element are quantified by projecting the phonon eigenvector ϕ to each of the atoms. For instance, the contribution from metal atoms is calculated as

$$|\phi_M|^2 = \sum_i |\phi_{i,x}|^2 + |\phi_{i,y}|^2 + |\phi_{i,z}|^2 \quad (1)$$

where $\phi_{i,\alpha}$ denotes the eigenvector of atom i in the α-direction and the sum goes over all metal atoms. Contributions of

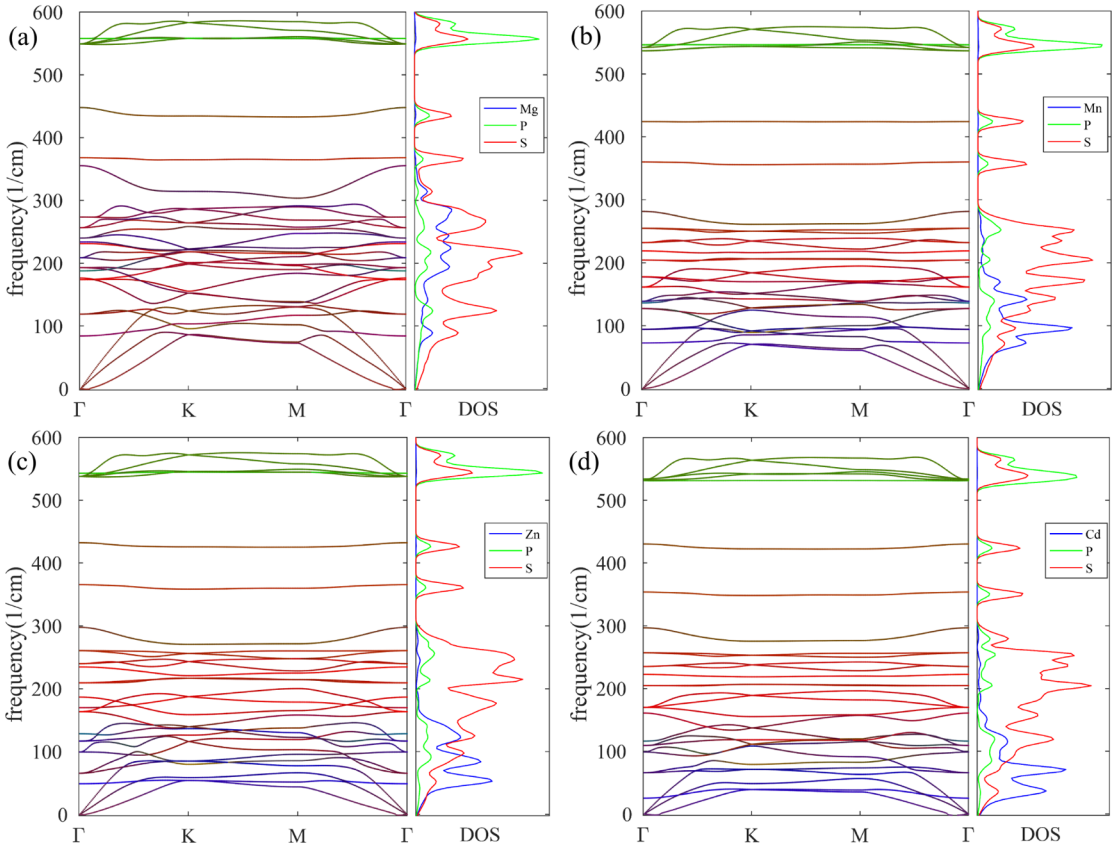

Figure 2. Phonon dispersion curves between high-symmetry points, Γ, K, M, together with the corresponding partial phonon DOSs: (a) $MgPS_3$, (b) $MnPS_3$, (c) $ZnPS_3$, and (d) $CdPS_3$. Blue, green, and red denote projection to metal, phosphorus, and chalcogen atoms, respectively.

DOI: 10.1021/acs.jpcc.7b09634
J. Phys. Chem. C 2017, 121, 27207−27217

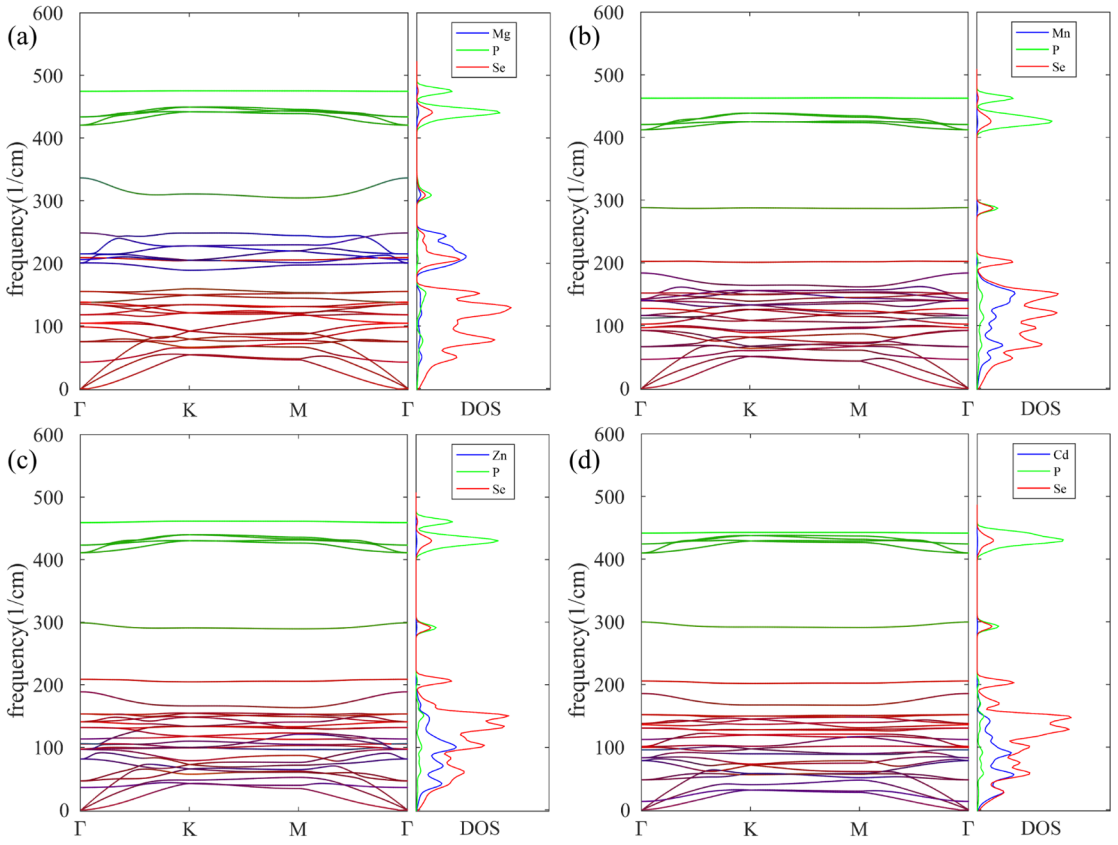

Figure 3. Phonon dispersion curves between high-symmetry points, Γ, K, M, together with the corresponding partial phonon DOSs: (a) $MgPSe_3$, (b) $MnPSe_3$, (c) $ZnPSe_3$, and (d) $CdPSe_3$. Blue, green, and red denote projection to metal, phosphorus, and chalcogen atoms, respectively.

phosphorus ($|\phi_P|^2$) and chalcogen ($|\phi_X|^2$) atoms are determined similarly. The contributions are normalized so that $|\phi_{tot}|^2 = |\phi_M|^2 + |\phi_P|^2 + |\phi_X|^2 = 1$. The atomic displacements for all Raman-active modes are presented in the Figure 6 in the case of $ZnPS_3$.

The dispersion curves show a few common features. First, since there are no imaginary frequency modes, all materials are dynamically stable. Second, as expected for 2D materials, there are two acoustic modes with linear q-dependences corresponding to the transversal and longitudinal modes within the plane, and one mode with a quadratic dependence describing the out-of-plane flexural response to the stress when one tries to bend the 2D plate. Third, all plots show similar orderings of the most significant atomic contributions as a function of the mode frequency. In MPS_3 (except M = Mg), the metal, chalcogen, and phosphorus contributions mostly play roles at low, middle, and high frequencies. When comparing materials of different elements, the shift of the frequencies can be intuitively understood on the basis of different atomic masses. The only exception seems to be the case of $MgPSe_3$, where the metal atoms are markedly lighter than the chalcogen atoms (Figure 3a). In more detail, there is (i) a manifold of states from 0 to 300 cm^{-1} in sulfides and from 0 to 200 cm^{-1} in selenides, (ii) two flat bands at around 370 and 430 cm^{-1} in sulfides and around 200 and 300 cm^{-1} in selenides, and (iii) a set of bands between 500 and 600 cm^{-1} in sulfides and between 400 and 500 cm^{-1} in selenides. Frequencies of both the flat bands and the high-frequency bands are largely independent of the metal atoms. The high-frequency bands originate from the vibrations of the P_2 dimer (cf. the displacements of modes A_{1g}^3 and E_g^5 in Figure 6). The two flat bands arise from breathing modes of the P_2S_6 cluster, where the chalcogen atoms in the top and bottom layer move either symmetrically (A_{1g}, lower frequency mode, cf. mode A_{1g}^3 in Figure 6) or antisymmetrically (A_{2u}, higher frequency mode).

Due to the zigzag AFM ordering in the case of $FePX_3$ and $NiPX_3$, the point group of the lattice is reduced to C_{2h} (cf. character table in Table 2), and due to the larger supercell the number of vibrational modes is 60. The irreducible representations at the Γ-point are $16A_g + 14A_u + 12B_g + 18B_u$, where the A_g and B_g modes are Raman-active, one A_u and two B_u modes are acoustic, and the remaining ones are IR-active. Nevertheless, the phonon dispersions plotted in Figure 4 show largely all the same features as discussed above. $FePS_3$ and $FePSe_3$ have few imaginary modes related to the breaking of the symmetry along the ferromagnetically coupled zigzag chain of Fe atoms, as mentioned in the methods section. The phonon dispersions for the distorted structures are shown in the Appendix for reference.

3.2. Nonresonant Raman Spectra. The Raman intensity I of a phonon mode is proportional to $|\mathbf{e}_s^T \cdot \mathbf{R} \cdot \mathbf{e}_i|^2$,[31] where $\mathbf{e}_s$ and $\mathbf{e}_i$ are the electric polarization vectors of the scattered and incident light, respectively, and superscript T of $\mathbf{e}_s$ denotes transpose. The Raman tensor $\mathbf{R}$ is a second rank tensor calculated as the derivative of the polarizability with respect to the normal mode coordinates.[32,33] The D_{3d} point symmetry group dictates that the Raman tensors for the A_{1g} and E_g active modes can be expressed as[31]

$$\mathbf{R}(A_{1g}) = \begin{bmatrix} a & \cdot & \cdot \\ \cdot & a & \cdot \\ \cdot & \cdot & b \end{bmatrix} \quad (2)$$

DOI: 10.1021/acs.jpcc.7b09634
J. Phys. Chem. C 2017, 121, 27207−27217

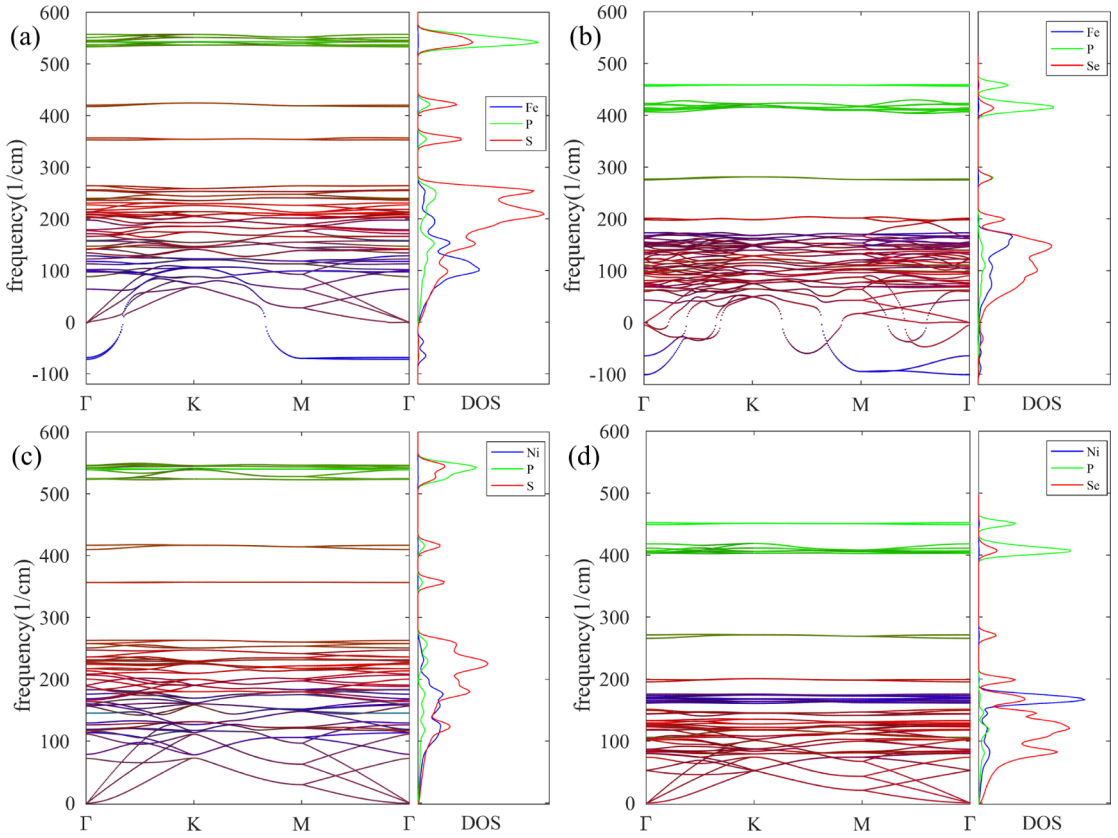

Figure 4. Phonon dispersion curves between high-symmetry points, Γ[0,0,0]:K[0.5,0.5,0]:M[0,0.5,0], together with the corresponding partial phonon DOSs: (a) $FePS_3$, (b) $FePSe_3$, (c) $NiPS_3$, and (d) $NiPSe_3$. Blue, green, and red denote projection to metal, phosphorus, and chalcogen atoms, respectively.

$$\mathbf{R}(\mathrm{E_g}) = \begin{bmatrix} \cdot & c & \cdot \\ c & \cdot & d \\ \cdot & e & \cdot \end{bmatrix}, \begin{bmatrix} c & \cdot & -d \\ \cdot & -c & \cdot \\ -e & \cdot & \cdot \end{bmatrix} \tag{3}$$

where a−e are the major terms. The other terms denoted by "·" are expected to be zero on the basis of symmetry, while a minor contribution may be obtained in calculations due to numerical inaccuracies.

As commonly adopted in Raman spectroscopy of 2D materials,[17,34] we consider the backscattering configuration, in which the incident light moves along the z-axis and the polarization vectors within the xy-plane are $\mathbf{e}_i^T = (\cos\theta, \sin\theta, 0)$ and $\mathbf{e}_s^T = (\cos\phi, \sin\phi, 0)$, where θ and ϕ, respectively, are the angles of the incident and scattered electric polarization vectors with x-axis in detectors. Thus

$$I(\mathrm{A_{1g}}) = a^2\cos^2(\phi - \theta)$$
$$I(\mathrm{E_g}) = c^2[\sin^2(\theta + \phi) + \cos^2(\theta + \phi)] = c^2 \tag{4}$$

Based on the above relations, A_{1g} modes depend on the polarization change between the incident and scattered light, but for E_g modes the angle dependence vanishes. In order to have the maximum possible amount of intensity for each mode, we fix the polarization vectors to the parallel configuration $\theta = \phi$, whereby $I(A_{1g}) = a^2$ and $I(E_g) = c^2$.

For the C_{2h} point group, the tensors are

$$\mathbf{R}(\mathrm{A_g}) = \begin{bmatrix} a & \cdot & d \\ \cdot & b & \cdot \\ d & \cdot & c \end{bmatrix} \tag{5}$$

$$\mathbf{R}(\mathrm{B_g}) = \begin{bmatrix} \cdot & e & \cdot \\ e & \cdot & f \\ \cdot & f & \cdot \end{bmatrix} \tag{6}$$

and the intensitites

$$I(\mathrm{A_g}) = |a\cos\theta\cos\phi + b\sin\theta\sin\phi|^2$$
$$I(\mathrm{B_g}) = |e\sin\theta\cos\phi + f\cos\theta\sin\phi|^2 \tag{7}$$

We note that even when we assume the parallel configuration $\theta = \phi$, the dependence on the polarization angle is retained when $a \neq b$. The calculated Raman spectra are shown in Figure 5 (with the artificial broadening of 4 cm^{-1} to mimic the experimental spectra), and the absolute values of I are listed in Table 3. Overall, a drastic sensitivity to the chalcogen anion is evident, whereas the spectra appear fairly insensitive to the metal cation, except for the two lowest E_g modes, which have the strongest contributions from the metal atoms.

The spectra of the D_{3d} systems are discussed next with the help of the schematic representations of the displacements shown in Figure 6 in the case of $ZnPS_3$. We start from the two low-frequency E_g Raman modes; E_g^1 corresponds to rotation of the P_2X_6 cluster and E_g^2 to an in-plane optical mode involving metal atoms. They are sensitive to the metal atom, but the Raman activities are small. Next, there is a group of two E_g modes and one A_{1g} mode, with medium Raman activities depending on the material. E_g^3 and E_g^4 modes correspond to the stretching of the P_2X_6 cluster and the A_{1g}^1 mode to a breathing mode involving chalcogen atoms displaced out-of-plane. The most intense

DOI: 10.1021/acs.jpcc.7b09634
J. Phys. Chem. C 2017, 121, 27207−27217

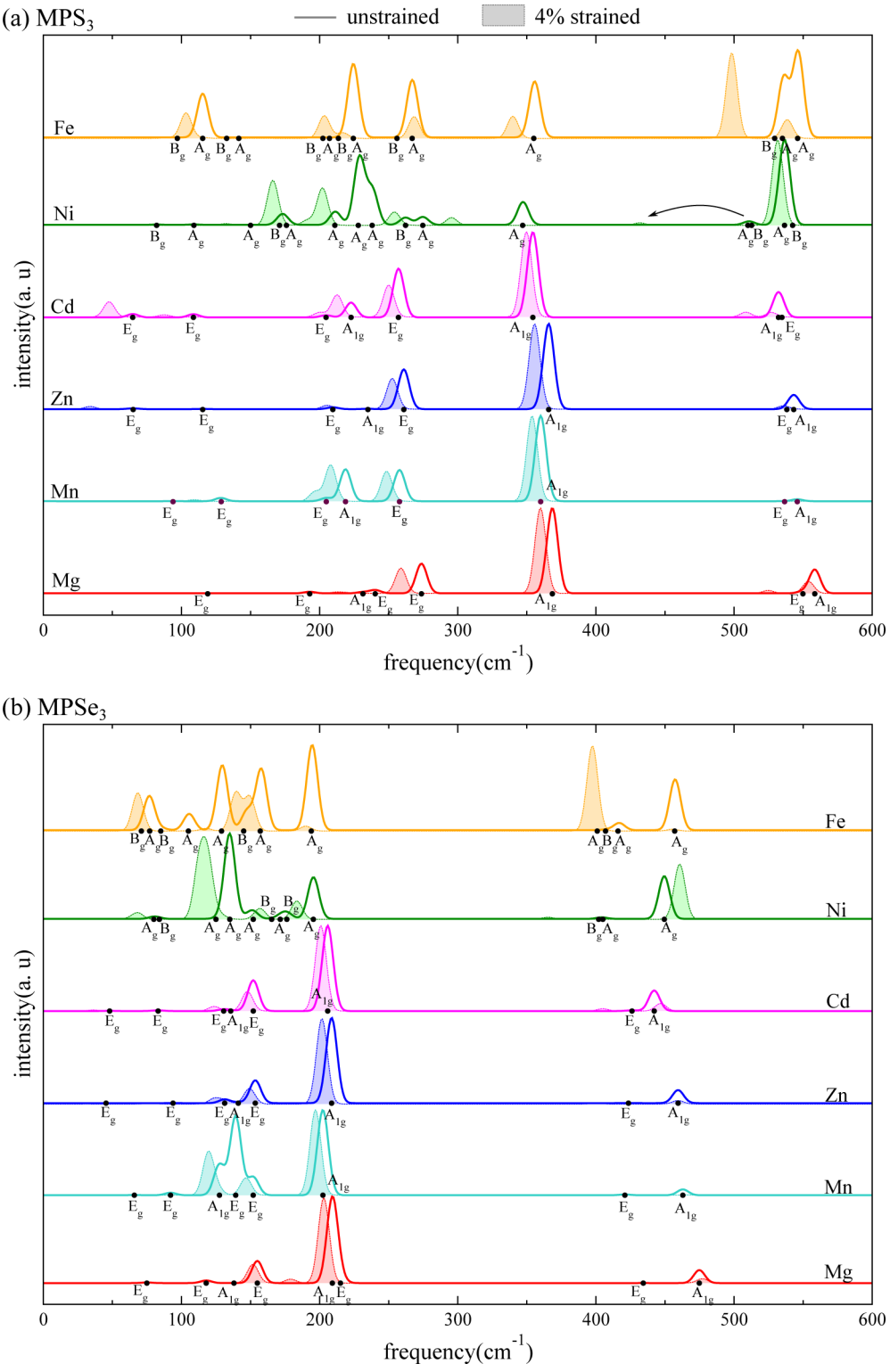

Figure 5. Normalized Raman spectra in the parallel configuration for (a) sulfides and (b) selenides, in the cases of both unstrained (solid line) and 4% strained (shaded regions) lattices. The dots depict frequencies that are expected to have Raman-active modes, and the corresponding irreducible representations are also denoted. The black arrow for $NiPS_3$ indicates the origin of the weak peak appearing at 430 cm^{-1}.

Raman peak is A_{1g}^2, which can be considered as a breathing mode of the P_2X_6 cluster. Finally, there are high-frequency modes including the P_2 stretching mode A_{1g}^3 with a medium activity and a low-activity E_g^5 mode corresponding to the rotation of the P_2 dimer.

Experimental data on monolayer TMPTs are still very scarce, but a comparison of our results with bulk spectra reveals an overall agreement. First of all, due to the underbinding by the PBE functional, as also seen in the overestimation of the lattice constants, the calculated frequencies are generally lower than the experimental values. In an early study,[35] Bernasconi et al. presented room temperature Raman spectra for $MnPS_3$, $NiPS_3$, $ZnPS_3$, $FePS_3$, and $FePSe_3$. All the sulfides showed strong peaks

DOI: 10.1021/acs.jpcc.7b09634
J. Phys. Chem. C 2017, 121, 27207−27217

Table 3. Frequencies ω, Raman Intensities I, and the Frequency Gradients $d\omega/d\epsilon$ for the Raman-Active Modes[a]

		$MgPS_3$	$MgPSe_3$	$MnPS_3$	$MnPSe_3$	$ZnPS_3$	$ZnPSe_3$	$CdPS_3$	$CdPSe_3$
A_{1g}^1	ω	230.9	137.9	218.7	127.4	234.9	141.1	222.7	135.6
	I	0.53	0.007	0.61	0.6	0.036	0.002	0.39	0.069
	$d\omega/d\epsilon$	−11.77	−0.62	−2.61	−4.22	−3.25	−1.52	−2.55	−1.86
A_{1g}^2	ω	368	209	360	202.3	365.7	208.6	354.3	205.8
	I	1.0	1.0	1.0	1.0	1.0	1.0	1.0	1.0
	$d\omega/d\epsilon$	−2.08	−1.55	−1.66	−1.33	−2.54	−1.72	−1.15	−1.18
A_{1g}^3	ω	557.9	474.6	545.8	462.9	543.1	459.4	532.1	442.1
	I	0.104	0.39	0.15	0.26	0.41	0.39	0.55	0.5
	$d\omega/d\epsilon$	−1.12	0.53	−0.49	1.66	−1.82	−0.02	−1.47	1.2
E_g^1	ω	118.8	74.9	93.9	65.8	65.1	45.4	64.7	47.9
	I	0.029	0.056	0.033	0.045	0.077	0.0003	0.16	0.034
	$d\omega/d\epsilon$	−5.21	−2.89	−2.75	−1.63	−7.52	−2.18	−4.39	−2.94
E_g^2	ω	192.9	117.8	128.7	92.07	115.3	93.8	108.6	83.1
	I	0.88	0.13	0.15	0.71	0.041	0.015	0.16	0.071
	$d\omega/d\epsilon$	−3.59	−0.05	−4.40	−0.11	−7.52	−4.03	−5.48	−2.86
E_g^3	ω	239.9	155	204.8	139.2	209.5	131.2	204.6	130.5
	I	0.15	0.15	0.016	0.14	0.1	0.17	0.055	0.1
	$d\omega/d\epsilon$	−5.31	−0.9	−1.86	−3.26	−1.04	−1.93	−1.24	−1.68
E_g^4	ω	273.5	214.9	254.8	151.8	260.9	153.4	257.1	151.9
	I	0.42	0.18	0.48	0.37	0.54	0.41	0.61	0.48
	$d\omega/d\epsilon$	−3.84	−9.02	−1.62	−1.29	−2.2	−1.09	−1.86	−1.06
E_g^5	ω	549.5	433.7	536.5	420.9	538.2	423.5	534.6	426.1
	I	0.114	0.013	0.022	0.076	0.01	0.03	0.036	0.048
	$d\omega/d\epsilon$	−6.27	−4.57	−6.69	−4.99	−8.12	−5.68	−6.71	−4.92

[a]The frequency shifts are in the units of $cm^{-1}/\%$.

at around 280 and 390 cm^{-1}, with the former accompanied by one or two weaker peaks at some tens of cm^{-1} lower wavenumbers. Based on our calculations, the pronounced peaks are assigned to E_g^4 and A_{1g}^2 modes, respectively, and the weaker features to E_g^3 and A_{1g}^1 modes. Peaks with smaller intensities were found below 200 cm^{-1}, likely corresponding to E_g^1 and E_g^2 modes, but varying from system to system, and weak features around 580 cm^{-1} corresponding to E_g^4 and A_{1g}^3 modes.

The overall good agreement with the experimental results for bulk systems is not surprising, as the vibrational modes are largely confined to the layers and there is little interaction between the layers. This has also been verified experimentally in few cases. For $NiPS_3$, Kuo et al. obtained the spectra for bulk and 2−7 layers,[36] showing little variation with respect to the number of layers. Similar conclusions were reached for $FePX_3$.[6,37] While less data is available for selenides, similar conclusions are expected to hold.

The calculated Raman spectra for the C_{2h} compounds, $FePX_3$ and $NiPX_3$, need to be discussed separately. Overall the results for symmetric $FePX_3$ are still largely in line with those for the D_{3d} compounds. The assignments become more complicated due to a larger number of Raman-active modes, but the most intense features are expected to arise from similar phonon modes. Moreover, these primary modes are found in both the symmetric and distorted phases, as presented in the Appendix.

The $NiPX_3$ spectra appear little different from the rest, even though the structures were found to be symmetric without imaginary frequency modes. The experimental results of Bernasconi et al. showed the same intense features as the other TMPTs but also several additional intense peaks below 200 cm^{-1} and between 400 and 600 cm^{-1}. In the calculated spectra, the high-frequency modes are in accordance with the other materials. In addition, we see several Raman active modes between 150 and 300 cm^{-1}, but it is difficult to assign these to the experimentally observed modes at this frequency range.

Raman spectroscopy is often used to probe the strain of the material, and thus we will next consider how Raman spectra change in response to the biaxial tensile strain. The shift of the Raman-active mode frequencies as a function of the applied strain are shown in Figure 7 in the case of $CdPS_3$ and $CdPSe_3$. Within the studied range of strain values (1−4%), the frequencies exhibit linear dependence on strain. The gradients of the frequencies $d\omega/d\epsilon$ are also listed in Table 3. In addition, the shaded regions in Figure 5 indicate Raman spectra of the materials under a 4% strain and give a quick visual indication of the changes. As expected, stretching weakens the bonds, and consequently the frequencies shift to lower wavenumbers. The only exception is the A_{1g}^3 mode in the case of selenides, which involves only out-of-plane movement of the P atoms (cf. Figure 6). Thus, the positive gradient could be rationalized such that the tensile strain leads to reduction of the layer thickness d, which consequently allows for strengthening of the P−P bond. The most prominent E_g^4 and A_{1g}^2 modes largely retain their intensities with frequency shifts of −1 to −4 cm^{-1} per 1% of strain and thus should be applicable for analyzing the strain of the sample. The magnitudes of these shifts are comparable to those found in other 2D materials. For instance, for monolayer MoS_2 upon application of biaxial strain, the E_{2g}^1 mode is shifted by −5.2 $cm^{-1}/\%$ and the A_{1g} mode by −1.7 $cm^{-1}/\%$.[38] Graphene, on the other hand, shows a much larger shift in the G-mode, i.e., −63 $cm^{-1}/\%$.[39]

3.3. Elastic Constants. To finalize our study on the mechanical properties of TMPT materials, we calculated the elastic tensor with three nontrivial independent coefficients C_{11}, C_{12}, and C_{44}. In addition, we determined $C_{shear} = (C_{11} - C_{12})/2$, $Y_s = (C_{11}^2 + C_{12}^2)/C_{11}$, $\nu = C_{12}/C_{11}$. The results are listed in Table 4. The selenides show consistently slightly smaller elastic

DOI: 10.1021/acs.jpcc.7b09634
J. Phys. Chem. C 2017, 121, 27207−27217

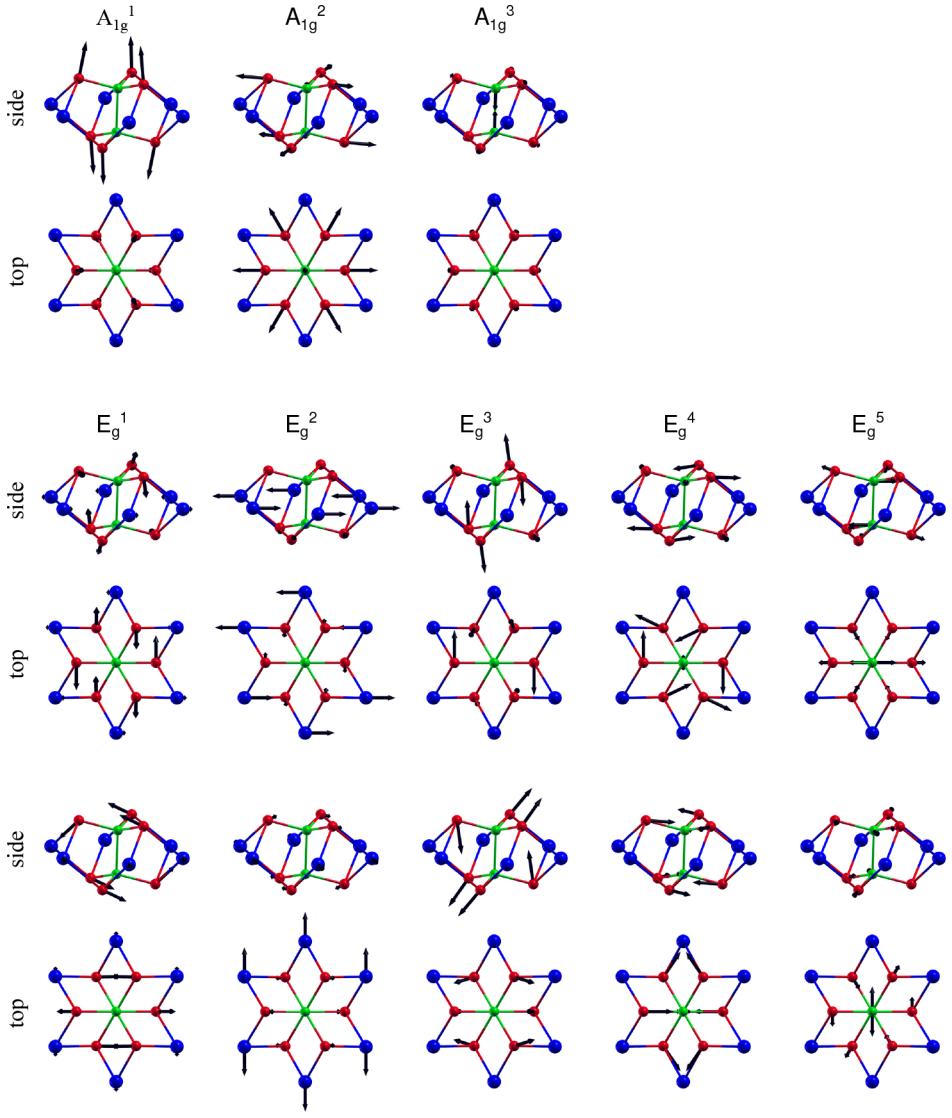

Figure 6. Schematic representations of atomic displacements of eight Raman-active modes as top and side views. The superscripts denote the indexing of the modes within the same symmetry. Two figures are shown for each of the doubly degenerate E_g modes. Blue, green, and red balls denote metal, phosphorus, and chalcogen atoms, respectively. Arrows are proportional to the displacements and come from the real part of the eigenvectors at the Γ-point. The sizes and orientations of the arrows correspond to the magnitudes and directions of the displacement vectors.

constants than the respective sulfides, but overall all TMPTs exhibit roughly similar values. More interestingly, a comparison with other 2D materials reveals that these materials are soft exhibiting, e.g., Young's modulus of roughly half of that for MoS_2 and one-fourth of that for graphene. Only MPX_3 and $NiPX_3$ show a ν values comparable to MoS_2, whereas all the other TMPTs show high Poisson ratios of 0.3−0.4.

4. CONCLUSIONS

We have carried out extensive first-principles calculations of the mechanical and vibrational properties of monolayer TMPTs MPX_3 (M = Mg, Mn, Fe, Ni, Zn, or Cd; X = S or Se). We analyzed their dynamical stabilities and atomic characters of the vibrational modes. The Raman spectra of the unstrained and strained layers were calculated, and the nature of the Raman active modes was discussed in detail. The softening rate of the modes upon strain can be used to identify the degree of strain in the samples measured experimentally. Finally, we assessed the elastic properties, showing that these materials are softer than many other layered materials, which should be taken into account to optimize the exfoliation process.

APPENDIX: COMPARISON BETWEEN THE SYMMETRIC AND DISTORTED STRUCTURES OF $FEPX_3$

The phonon dispersions from the symmetric and distorted structures are shown in Figure 8 for $FePS_3$ and $FePSe_3$. The symmetric structure shows few imaginary modes, which correspond to breaking of the symmetry in the Fe−Fe bonds along the zigzag chain of parallel magnetic moments (cf. the rectangular unit cell in Figure 1). The distorted structures, obtained by displacing the atoms according to these imaginary modes and relaxing the structure again, are free of imaginary modes. The high-frequency modes, originating either from the P_2 or P_2X_6 displacements, are only weakly affected by the distortion involving the Fe−Fe bonds.

DOI: 10.1021/acs.jpcc.7b09634
J. Phys. Chem. C 2017, 121, 27207−27217

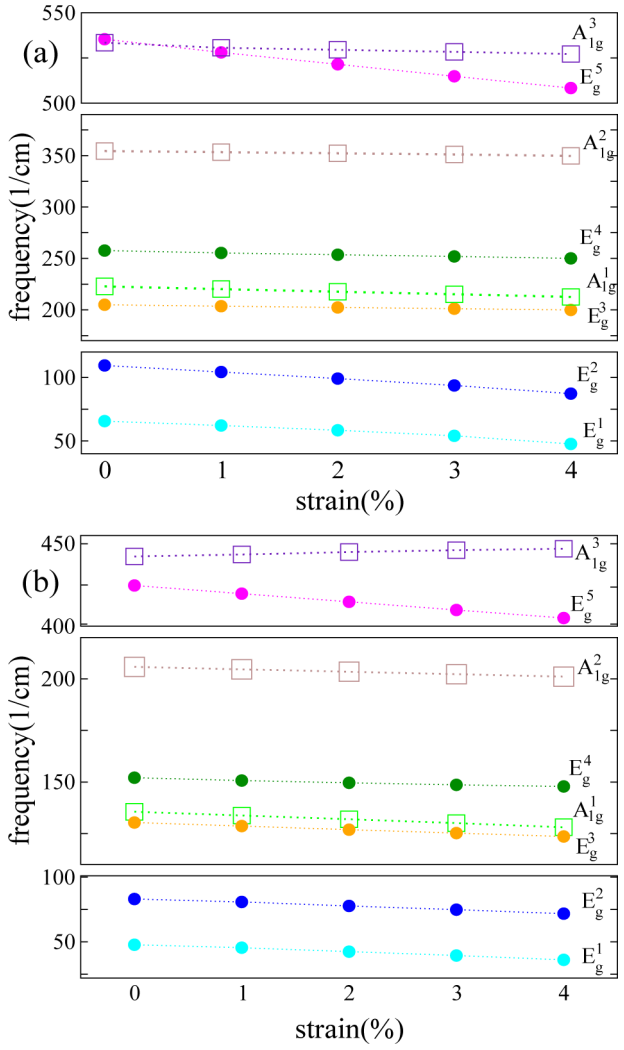

Figure 7. Effect biaxial strain (0–4%) on the frequencies of Raman-active modes: (a) $CdPS_3$ and (b) $CdPSe_3$. The slope of the linear fitting for all the materials and modes is reported in Table 1.

Table 4. Calculated Elastic Constants and Comparison to Few Other Common 2D Materials[a]

	C_{11}	C_{12}	C_{shear}	Y_s	ν
$MgPS_3$	65.4	17.4	24.0	70.0	0.266
$MgPSe_3$	55.7	15.4	20.1	59.9	0.277
$MnPS_3$	61.7	20.2	20.8	68.3	0.327
$MnPSe_3$	53.2	18.6	17.3	59.7	0.350
$FePS_3$	72.7	22.1	25.0	79.4	0.304
$FePSe_3$	61.9	19.4	22.0	67.9	0.312
$NiPS_3$	87.0	23.1	31.9	93.1	0.265
$NiPSe_3$	73.3	20.1	26.7	78.8	0.275
$ZnPS_3$	67.5	27.1	20.2	78.4	0.401
$ZnPSe_3$	58.3	22.9	17.7	67.4	0.393
$CdPS_3$	53.6	20.6	16.5	61.6	0.385
$CdPSe_3$	47.0	17.9	14.5	53.8	0.381
MoS_2	137.9	36.0	50.9	147.3	0.262
graphene	352.6	59.6	146.5	362.67	0.17

[a]Elastic constant C_{11}, C_{12}, and Young's modulus Y_s are in the units of N/m. The Poisson ratio ν is unitless.

Comparison of the calculated (PBE) Raman spectra of the symmetric and distorted structures for the $FePS_3$ monolayer to the experimental ones[6] is presented in Figure 9. The highest peak is not recorded in the experimental spectrum. In addition, the results from PBE+*U* calculations are shown, where a *U* parameter of 3.5 eV is used for the Fe d orbitals. The parameter was chosen to yield the same energy difference

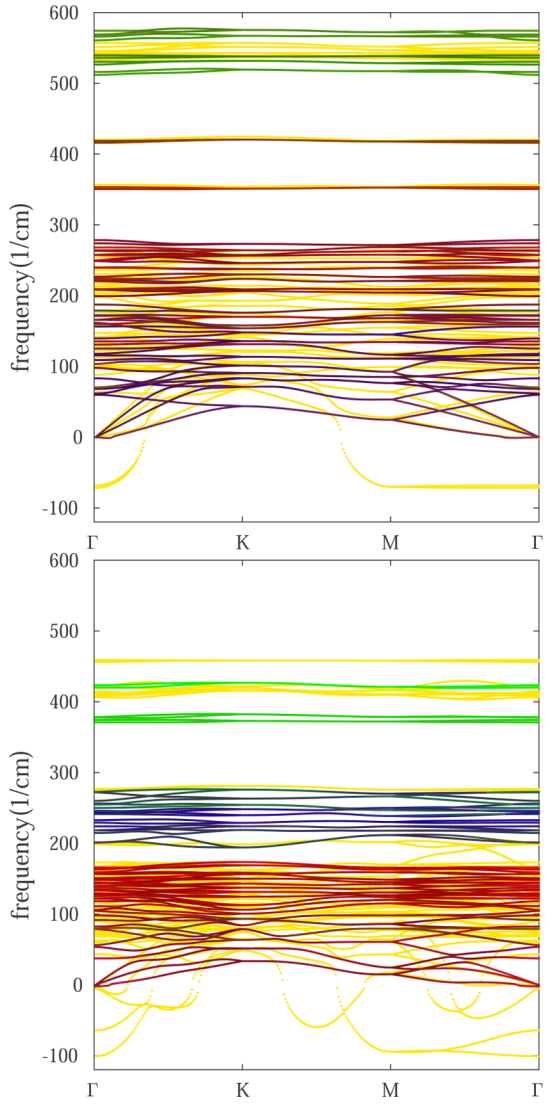

Figure 8. Comparison of the phonon dispersion curves for $FePS_3$ (top) and $FePSe_3$ (bottom) in the symmetric and distorted structures. The symmetric ones are the same as shown in Figure 4a, b and colored by yellow. The distorted structure is colored according to the projection to the atoms as previously.

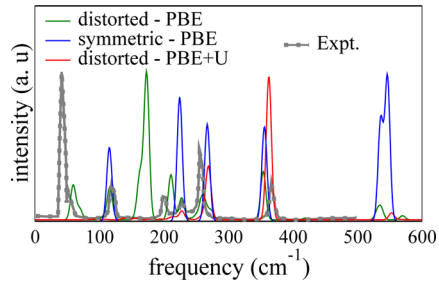

Figure 9. Comparison of the experimental Raman spectra of $FePS_3$ (data from ref 6) with the calculated ones from distorted and symmetric structures and also calculated using the PBE+*U* method.

DOI: 10.1021/acs.jpcc.7b09634
J. Phys. Chem. C 2017, 121, 27207–27217

between the FM and AFM configurations as in HSE calculations. Such a choice also almost completely removes the distortion. The main peaks at around 250 and 350 cm^{-1} are found in all calculated spectra. The distorted structure gives perhaps a better overall agreement with the experimental spectra but also yields an intense extra feature at around 170 cm^{-1}. The symmetric structure, on the other hand, fails to reproduce the peak at around 50 cm^{-1} and shows only two peaks between 200 and 300 cm^{-1} instead of three. The PBE+U approach seems to overall perform the worst. All the low-frequency modes below 200 cm^{-1} are either missing or show very small intensity. On the other hand, the third peak at around 200 cm^{-1} is present, although with weak intensity.

AUTHOR INFORMATION

Corresponding Authors

*E-mail: arsalan.hashemi@aalto.fi.

*E-mail: hannu-pekka.komsa@aalto.fi.

ORCID

Hannu-Pekka Komsa: 0000-0002-0970-0957

Martti Puska: 0000-0002-8419-3289

Arkady V. Krasheninnikov: 0000-0003-0074-7588

Notes

The authors declare no competing financial interest.

ACKNOWLEDGMENTS

We thank the Academy of Finland for the support under Project No. 286279, and through its Centres of Excellence Programme (2012-2017) under Project No. 251748. We also thank CSC-IT Center for Science Ltd. and Aalto Science-IT project for generous grants of computer time.

REFERENCES

(1) Li, X.; Cao, T.; Niu, Q.; Shi, J.; Feng, J. Coupling the Valley Degree of Freedom to Antiferromagnetic Order. *Proc. Natl. Acad. Sci. U.S.A.* **2013**, *110*, 3738−3742.

(2) Ressouche, E.; Loire, M.; Simonet, V.; Ballou, R.; Stunault, A.; Wildes, A. Magnetoelectric MnPS3 as a Candidate for Ferrotoroidicity. *Phys. Rev. B: Condens. Matter Mater. Phys.* **2010**, *82*, 100408.

(3) Wildes, A. R.; Rule, K. C.; Bewley, R. I.; Enderle, M.; Hicks, T. J. The Magnon Dynamics and Spin Exchange Parameters af FePS3. *J. Phys.: Condens. Matter* **2012**, *24*, 416004.

(4) Liu, J.; Li, X.-B.; Wang, D.; Lau, W.-M.; Peng, P.; Liu, L.-M. Diverse and Tunable Electronic Structures of Single-Layer Metal Phosphorus Trichalcogenides for Photocatalytic Water Splitting. *J. Chem. Phys.* **2014**, *140*, 054707.

(5) Wildes, A. R.; Rønnow, H. M.; Roessli, B.; Harris, M. J.; Godfrey, K. W. Static and Dynamic Critical Properties of the Quasi-Two-Dimensional Antiferromagnet MnPS3. *Phys. Rev. B: Condens. Matter Mater. Phys.* **2006**, *74*, 094422.

(6) Du, K.-z.; Wang, X.-z.; Liu, Y.; Hu, P.; Utama, M. I. B.; Gan, C. K.; Xiong, Q.; Kloc, C. Weak van der Waals Stacking, Wide-Range Band Gap, and Raman Study on Ultrathin Layers of Metal Phosphorus Trichalcogenides. *ACS Nano* **2016**, *10*, 1738−1743.

(7) Kuo, C.-T.; Neumann, M.; Balamurugan, K.; Park, H. J.; Kang, S.; Shiu, H. W.; Kang, J. H.; Hong, B. H.; Han, M.; Noh, T. W.; Park, J.-G.; et al. Exfoliation and Raman Spectroscopic Fingerprint of Few-Layer $NiPS_3$ van der Waals Crystals. *Sci. Rep.* **2016**, *6*, 20904.

(8) Py, M. A.; Haering, R. R. Structural Destabilization Induced by Lithium Intercalation in MoS2 and Related Compounds. *Can. J. Phys.* **1983**, *61*, 76−84.

(9) Chhowalla, M.; Shin, H. S.; Eda, G.; Li, L.-J.; Loh, K. P.; Zhang, H. The Chemistry of Two-Dimensional Layered Transition Metal Dichalcogenide Nanosheets. *Nat. Chem.* **2013**, *5*, 263−275.

(10) Joy, P. A.; Vasudevan, S. Magnetism in the Layered Transition-Metal Thiophosphates MPS3 (M = Mn, Fe, And Ni). *Phys. Rev. B: Condens. Matter Mater. Phys.* **1992**, *46*, 5425−5433.

(11) Ouvrard, G.; Brec, R.; Rouxel, J. Structural Determination of Some MPS3 Layered Phases (M = Mn, Fe, Co, Ni And Cd). *Mater. Res. Bull.* **1985**, *20*, 1181−1189.

(12) Zhang, X.; Zhao, X.; Wu, D.; Jing, Y.; Zhou, Z. MnPSe3 Monolayer: A Promising 2D Visible-Light Photohydrolytic Catalyst with High Carrier Mobility. *Advanced Science* **2016**, *3*, 1600062.

(13) Sivadas, N.; Okamoto, S.; Xiao, D. Gate-Controllable Magneto-Optic Kerr Effect in Layered Collinear Antiferromagnets. *Phys. Rev. Lett.* **2016**, *117*, 267203.

(14) Li, X.; Wu, X.; Yang, J. Half-Metallicity in MnPSe3 Exfoliated Nanosheet with Carrier Doping. *J. Am. Chem. Soc.* **2014**, *136*, 11065−11069.

(15) Gusmão, R.; Sofer, Z.; Sedmidubský, D.; Huber, Š.; Pumera, M. The Role of the Metal Element in Layered Metal Phosphorus Triselenides upon Their Electrochemical Sensing and Energy Applications. *ACS Catal.* **2017**, *7*, 8159−8170.

(16) Lee, J.-U.; Lee, S.; Ryoo, J. H.; Kang, S.; Kim, T. Y.; Kim, P.; Park, C.-H.; Park, J.-G.; Cheong, H. Ising-Type Magnetic Ordering in Atomically Thin FePS3. *Nano Lett.* **2016**, *16*, 7433−7438.

(17) Zhang, X.; Qiao, X.-F.; Shi, W.; Wu, J.-B.; Jiang, D.-S.; Tan, P.-H. Phonon and Raman Scattering of Two-Dimensional Transition Metal Dichalcogenides from Monolayer, Multilayer to Bulk Material. *Chem. Soc. Rev.* **2015**, *44*, 2757−2785.

(18) Parkin, W. M.; Balan, A.; Liang, L.; Das, P. M.; Lamparski, M.; Naylor, C. H.; Rodríguez-Manzo, J. A.; Johnson, A. T. C.; Meunier, V.; Drndić, M. Raman Shifts in Electron-Irradiated Monolayer MoS2. *ACS Nano* **2016**, *10*, 4134−4142.

(19) Eckmann, A.; Felten, A.; Mishchenko, A.; Britnell, L.; Krupke, R.; Novoselov, K. S.; Casiraghi, C. Probing the Nature of Defects in Graphene by Raman Spectroscopy. *Nano Lett.* **2012**, *12*, 3925−30.

(20) Scheuschner, N.; Gillen, R.; Staiger, M.; Maultzsch, J. Interlayer Resonant Raman Modes in Few-Layer MoS2. *Phys. Rev. B: Condens. Matter Mater. Phys.* **2015**, *91*, 235409.

(21) Sheremetyeva, N.; Cherniak, D. J.; Watson, E. B.; Meunier, V. Effect of pressure on the Raman-active modes of zircon (ZrSiO4): A first-principles study. *Phys. Chem. Miner.* **2017**, 1−12.

(22) Boucher, F.; Evain, M.; Brec, R. Second Order Jahn-Teller Eeffect in CdPS3 and ZnPS3 Demonstrated by a Non-harmonic Behaviour of Cd^{2+} and Zn2+ d10 Ions. *J. Alloys Compd.* **1994**, *215*, 63−70.

(23) Jörgens, S.; Mewis, A. Die Kristallstrukturen Von Hexachalcogeno-Hypodiphosphaten Des Magnesiums Und Zinks. *Z. Anorg. Allg. Chem.* **2004**, *630*, 51−57.

(24) Zeng, R.; Wang, S. Q.; Du, G. D.; Wang, J. L.; Debnath, J. C.; Shamba, P.; Fang, Z. Y.; Dou, S. X. Abnormal Magnetic Behaviors and Large Magnetocaloric Effect in MnPS3 Nanoparticles. *J. Appl. Phys.* **2012**, *111*, 07E144.

(25) Kresse, G.; Hafner, J. Ab-Initio Molecular Dynamics for Liquid Metals. *Phys. Rev. B: Condens. Matter Mater. Phys.* **1993**, *47*, 558−561.

(26) Rule, K. C.; McIntyre, G. J.; Kennedy, S. J.; Hicks, T. J. Single-Crystal and Powder Neutron Diffraction Experiments on FePS3: Search for the Magnetic Structure. *Phys. Rev. B: Condens. Matter Mater. Phys.* **2007**, *76*, 134402.

(27) Perdew, J. P.; Burke, K.; Ernzerhof, M. Generalized Gradient Approximation Made Simple. *Phys. Rev. Lett.* **1996**, *77*, 3865−3868.

(28) Chittari, B. L.; Park, Y.; Lee, D.; Han, M.; MacDonald, A. H.; Hwang, E.; Jung, J. Electronic and Magnetic Properties of Single-Layer MPX3Metal Phosphorous Trichalcogenides. *Phys. Rev. B: Condens. Matter Mater. Phys.* **2016**, *94*, 184428.

(29) Baroni, S.; de Gironcoli, S.; Dal Corso, A.; Giannozzi, P. Phonons and Related Crystal Properties from Density-Functional Perturbation Theory. *Rev. Mod. Phys.* **2001**, *73*, 515−562.

(30) Togo, A.; Tanaka, I. First-Principles Phonon Calculations in Materials Science. *Scr. Mater.* **2015**, *108*, 1−5.

(31) Cardona, M. *Light Scattering in Solids−I*; Springer: Berlin, 1983; Chapter 2.

DOI: 10.1021/acs.jpcc.7b09634
J. Phys. Chem. C 2017, 121, 27207−27217

(32) Fonari, A.; Stauffer, S. *Vasp_raman.py*; https://github.com/raman-sc/VASP/, 2013.
(33) Porezag, D.; Pederson, M. R. Infrared Intensities and Raman-Scattering Activities within Density-Functional Theory. *Phys. Rev. B: Condens. Matter Mater. Phys.* **1996**, *54*, 7830−7836.
(34) Saito, R.; Tatsumi, Y.; Huang, S.; Ling, X.; Dresselhaus, M. S. Raman Spectroscopy of Transition Metal Dichalcogenides. *J. Phys.: Condens. Matter* **2016**, *28*, 353002.
(35) Bernasconi, M.; Marra, G. L.; Benedek, G.; Miglio, L.; Jouanne, M.; Julien, C.; Scagliotti, M.; Balkanski, M. Lattice Dynamics of Layered MPX3 (M = Mn,Fe,Ni,Zn; X = S,Se) Compounds. *Phys. Rev. B: Condens. Matter Mater. Phys.* **1988**, *38*, 12089−12099.
(36) Kuo, C.-T.; Neumann, M.; Balamurugan, K.; Park, H. J.; Kang, S.; Shiu, H. W.; Kang, J. H.; Hong, B. H.; Han, M.; Noh, T. W.; Park, J.-G.; et al. Exfoliation and Raman Spectroscopic Fingerprint of Few-Layer NiPS3 van der Waals Crystals. *Sci. Rep.* **2016**, *6*, 20904.
(37) Lee, J.-U.; Lee, S.; Ryoo, J. H.; Kang, S.; Kim, T. Y.; Kim, P.; Park, C.-H.; Park, J.-G.; Cheong, H. Ising-Type Magnetic Ordering in Atomically Thin FePS3. *Nano Lett.* **2016**, *16*, 7433−7438.
(38) Lloyd, D.; Liu, X.; Christopher, J. W.; Cantley, L.; Wadehra, A.; Kim, B. L.; Goldberg, B. B.; Swan, A. K.; Bunch, J. S. Band Gap Engineering with Ultralarge Biaxial Strains in Suspended Monolayer MoS2. *Nano Lett.* **2016**, *16*, 5836−5841.
(39) Mohiuddin, T. M. G.; Lombardo, A.; Nair, R. R.; Bonetti, A.; Savini, G.; Jalil, R.; Bonini, N.; Basko, D. M.; Galiotis, C.; Marzari, N.; Novoselov, K. S.; Geim, A. K.; Ferrari, A. C.; et al. Uniaxial Strain in Graphene by Raman Spectroscopy: *g*-Peak Splitting, Grüneisen Parameters, and Sample Orientation. *Phys. Rev. B: Condens. Matter Mater. Phys.* **2009**, *79*, 205433.

DOI: 10.1021/acs.jpcc.7b09634
J. Phys. Chem. C 2017, 121, 27207−27217